THE JOURNAL OF PHYSICAL CHEMISTRY C
A JOURNAL OF THE AMERICAN CHEMICAL SOCIETY

pubs.acs.org/JPCC

Article

Optimized Titanium Nitride Epitaxial Film for Refractory Plasmonics and Solar Energy Harvesting

Ragini Mishra, Ching-Wen Chang, Abhishek Dubey, Zong-Yi Chiao, Ta-Jen Yen, Ho Wai Howard Lee, Yu-Jung Lu, and Shangjr Gwo*

Cite This: J. Phys. Chem. C 2021, 125, 13658−13665

Read Online

ACCESS | Metrics & More | Article Recommendations | Supporting Information

ABSTRACT: Titanium nitride (TiN) is an emerging material for refractory plasmonics owing to its excellent optical properties in the visible and near-infrared regions, high melting temperature, extreme mechanical hardness, and stability against material degradation in tough environments. Recently, TiN plasmonic metasurfaces have been proposed as optical broadband absorbers and narrow-band thermal emitters, which are critical for high-efficiency solar thermophotovoltaics. Here, we demonstrate a single-layer metasurface broadband absorber made from the oxidation-resistant TiN(111) epitaxial film grown on c-plane sapphire by nitrogen-plasma-assisted molecular beam epitaxy (MBE) with ∼90% absorptivity over the visible spectrum. This is accomplished by optimized plasmonic characteristics of the oxygen-free stoichiometric TiN film grown by MBE, in comparison with titanium oxynitride (TiO_xN_y) films prepared by the conventional reactive sputtering technique. In addition, the superb thermal and chemical stabilities of MBE-grown TiN metasurface are confirmed by vacuum annealing at 850 °C and irradiation under 130 suns in the ambient environment.

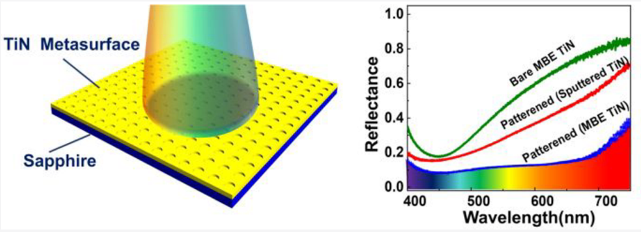

■ INTRODUCTION

In solar cell applications, the Shockley−Queisser (SQ) limit is a theoretical upper bound of solar energy conversion efficiency using a single-semiconductor p−n junction, which is 41% for maximum sunlight concentration and 31% without concentration.[1] The SQ limitation originates from the broadband nature of the solar spectrum and the semiconductor bandgap: While photons are not absorbed if the incident photon energy is less than the semiconductor bandgap, photons with energy greater than the bandgap are absorbed with some energy loss due to fast electron−hole pair relaxation to the band edges.

To overcome this limitation (broad solar spectrum), the concept of the solar thermophotovaltic (STPV) system has been proposed and demonstrated by including an intermediate light absorption (broadband)/emission (narrowband) element between the sunlight and the solar cell.[2−11] In essence, this intermediate element acts as an alternative "Sun" for solar cells,[7] which can absorb the entire solar spectrum and be heated to emit a narrowband spectrum tailored to match with the desired semiconductor photovoltaic element. The utmost advantage of STPV is that virtually all solar energy is converted into electrical energy, and an ideal intermediate element can tremendously boost the overall conversion efficiency. Based on a simple thermodynamic model,[11−13] the maximum STPV efficiency ($\eta_{\max}$) could be estimated by

$$\eta_{\max} = \left(1 - \frac{T^4}{T_s^4}\right)\left(1 - \frac{T_a}{T}\right) \qquad (1)$$

where the first factor is the blackbody radiative exchange between the intermediate element (temperature: T) and the Sun (temperature: T_s), and the second factor is the Carnot efficiency for a solar cell operating at the ambient temperature (T_a). Similar to the SQ limit, the theoretical maximum efficiency shown in eq 1 is only for an ideal system. However, it is widely adopted because of the possibility to determine the optimal temperature of the intermediate element for light absorption/emission between the sunlight and the solar cell. For example, assuming T_s = 6000 K and T_a = 300 K, the ideal STPV system could attain a maximum efficiency of 85%, which occurs when the intermediate blackbody is at the optimal temperature of T = 2544 K. In practice, it is difficult to operate at this temperature, and a conversion efficiency as high as 70% could be achieved at a moderate temperature of 1000 K,[11] which is already much better than the SQ limit.

However, the progress of the SPTV system has been slow due to the lack of reliable and sustainable optical materials which can operate at these high temperatures and other practical constraints. The best result reported to date is 3.2% (light-to-electricity efficiency) using a broadband absorber

Received: April 5, 2021
Revised: May 19, 2021
Published: June 9, 2021

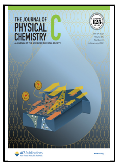

https://doi.org/10.1021/acs.jpcc.1c03053

("dark" absorber) made of vertically aligned multiple-walled carbon nanotubes, which is heated to ~1300 K.[7] Furthermore, due to the propensity of material degradation (e.g., oxidation) at high temperatures, a vacuum or inertia-gas-sealed environment is necessary for SPTV devices. Recent advances in plasmonics and low-loss refractory plasmonic materials have provided new perspectives for SPTV developments.[14−16] Especially, it has been theoretically proposed and experimentally demonstrated that titanium nitride (TiN) is a candidate refractory plasmonic material for building optical broadband absorption and narrowband emitters operating at high temperatures.[17−21] Partly, this is due to the excellent electronic and optical properties of TiN, such as low interband losses, high electrical conductivity, and comparable optical properties to gold in the visible and near-infrared spectral regions.[22−31] Nevertheless, the advantages of TiN are not only its ability to act as an alternative plasmonic material to gold but also its excellent thermal (high thermal conductivity and melting temperature),[16,32−36] mechanical strength (extreme hardness),[16,26] chemical stability against material degradation in tough environments,[37,38] complementary metal-oxide-semiconductor (CMOS) compatibility, and low material cost. In particular, TiN has been considered as the best candidate material for applications in photothermal energy conversion over a broad spectral region of the solar spectrum. According to a recent theoretical study,[26] nanostructured TiN is an excellent broadband sunlight absorber due to strong plasmonic resonance ranging from 300 to 1300 nm, corresponding to the major sunlight spectral composition.

One of the major challenges for TiN-based plasmonic devices is oxygen contamination in the grown TiN films since the O and N exchange reaction is thermodynamically favorable. For most of the plasmonic applications demonstrated so far, TiN films are deposited by reactive sputtering or chemical vapor deposition, which is not performed under the preferred ultrahigh vacuum conditions. Therefore, oxygen contamination is a major issue,[39−42] which could cause degradation of film properties, such as electrical resistivity, optical response, and thermal stability. In this work, we show that epitaxial growth of the oxidation-resistant TiN(111) film on sapphire by nitrogen-plasma-assisted molecular beam epitaxy (MBE) provides an optimized approach for refractory plasmonics requiring excellent plasmonic properties, as well as high thermal and chemical stabilities. Especially, a single-TiN-layer (~200 nm thick) metasurface broadband absorber with ~90% absorptivity over the visible spectrum is demonstrated. Furthermore, we show that the metasurface absorber made from the MBE-grown TiN film could sustain vacuum annealing at 850 °C and irradiation under 130 suns in the ambient environment without appreciable degradation in optical response and structural integrity. In comparison, the same absorber structure made from the sputtered TiN film shows inferior optical performance, as well as degraded thermal and chemical stabilities due to a significant amount of oxygen contamination in the film.

■ METHODS

TiN Epitaxial Growth. The MBE TiN film was grown by using a nitrogen-plasma-assisted molecular beam epitaxy system (DCA Instruments Oy) on a 2 in. c-plane sapphire wafer. The base pressure was ~1×10^{-10} Torr before the MBE growth, and we cleaned the sapphire wafer *in situ* by annealing at 900 °C for 1 h and raised the substrate temperature to 950 °C (growth temperature) for 1 h. Afterward, nitridation of sapphire was performed by using a nitrogen radio frequency (RF) plasma source (Veeco UNI-Bulb). The same nitrogen plasma source was also used during growth, the Ti flux was supplied by a high-temperature Knudsen cell, and the MBE TiN deposition rate was about 20 nm/h. For comparison, the sputtered TiN film was deposited by a reactive sputtering system (Kao Duen Technology Corporation) using a Ti target and Ar/N_2 gas (background pressure: ~3×10^{-8} Torr). The growth temperature was 800 °C, and the TiN deposition rate was ~60 nm/h.

XRD, SEM, and XPS Characterization. High-resolution X-ray diffraction (XRD) patterns of TiN films were acquired by using an X-ray diffractometer (Bede, D1) with a Cu $K_{\alpha 1}$ (1.54056 Å) X-ray source. Scanning electron microscopy (SEM) images of TiN films and metasurfaces were taken by a high-resolution field emission scanning electron microscope (JEOL, JSM 7500F). X-ray photoelectron spectroscopy (XPS) spectra were obtained by a scanning XPS microprobe system (ULVAC-PHI, PHI Quantera II) using Al K_α X-ray emission (photon energy $h\nu$ = 1486.6 eV).

Fabrication of TiN Metasurface Absorbers. Plasmonic metasurface absorbers were fabricated on MBE-grown and sputtered TiN-on-sapphire chips (1×1 cm^2) with an active (patterned) area of 50×50 μm^2. First, we cleaned the chips with acetone, isopropyl alcohol, and deionized water in an ultrasonic sonicator. Electron beam lithography was performed using an ELIONIX system (ELS-7500EX). Then, we spin-coated a poly(methyl methacrylate) (PMMA) positive resist. Afterwards, a conductive polymer (ESPACER 300Z) was spin-coated and baked at 80 °C for 3 min to prevent the electron-beam charging effects. Finally, patterned transfer was conducted by reactive ion etching (RIE) using a transformer-coupled plasma system (LAM Research, TCP9600). The same lithography procedure was followed for all samples to compare the results directly.

Optical Measurements. Optical reflection measurements of TiN metasurfaces in the visible spectral range were performed by a homemade setup. We used a tungsten halogen white-light lamp (Ocean Optics, HL-2000) for the reflectance measurements by collecting the reflected light through a 100× objective lens (N.A. = 0.82, OLYMPUS). The reflected light was then sent to a fiber-coupled spectrometer (Andor-Shamrock, SR-500i) for spectral analysis. For the polarization-dependent reflection measurement, the angle of incidence light was fixed, whereas the sample was rotated from 0° to 360° with an increment of 10°. The spectroscopic ellipsometry (SE) data were acquired by using a commercial spectroscopic ellipsometer (J. A. Woollam M-2000). The complex dielectric functions of both MBE and sputtered TiN films were extracted by fitting the SE data using the Drude–Lorentz model and a TiN/sapphire two-layer structure.

Irradiation of Sunlight and High-Temperature Annealing. The TiN metasurface samples were irradiated using a solar simulator (Newport, SP1000-5098), and the solar power was measured by an optical power meter (Newport, 1918-R). In addition, high-temperature vacuum annealing was performed by using the sputtering system. First, the annealed sample was loaded inside the chamber, and the sample temperature was raised with a ramping rate of ~150 °C/h. When the final temperature was reached at 850 °C, the TiN metasurface samples were annealed for 6 h. Afterwards, reflectance spectra were measured for direct comparison, and metasurface morphologies after annealing were examined by SEM.

FDTD Simulations. A commercial software package (Lumerical, FDTD solutions) was used for finite-difference time-domain (FDTD) simulations. The simulations were executed with a three-dimensional setup of the nanohole system using a 0.5 nm resolution grid. For the metasurface absorber simulations, the operating range of the plane wave source was from 400 to 800 nm. The incident light was a linearly polarized (along the x-direction) plane wave illuminated on the metasurface along the z-axis direction. A perfectly matched layer along the z-axis was used for the boundary condition, and periodic boundaries were adopted for both x- and y-axes.

■ RESULTS AND DISCUSSION

In this study, the (111)-oriented TiN epitaxial film (~200 nm thick) with a close-packed, rock-salt crystal structure is grown on a 2 in. (0001)-oriented (c-plane) sapphire wafer, and *in situ* streaky reflection high-energy electron diffraction (RHEED) patterns during and after the growth process indicate the smooth crystalline nature of the MBE TiN film. In comparison to (001) and (110) orientations, a recent study has demonstrated that the (111)-oriented TiN is more resistant to oxidation, even under a high oxygen partial pressure at 800 °C.[42] To compare with the oxygen-free stoichiometric film grown by MBE, a sputtered (111)-oriented TiN epitaxial film is also prepared by reactive sputtering on c-plane sapphire, and the same metasurface structure is used for a direct comparison. As a simple inspection approach, the absence or presence of oxygen contamination can be judged by the film color and carrier concentration.[30,42] The MBE TiN film exhibits a brilliant golden color, as shown in Figure 1a, and has a free electron concentration as high as 9 × 10^{22} cm^{-3}.[30] Furthermore, *ex situ* XRD measurements (Figure 1b) reveal that the full width half maxima (FWHM) of the MBE and sputtered TiN(111) peaks are 0.25° and 0.55°, respectively. Based on the XPS analysis, the wider XRD peak data are due to the inadvertent oxygen uptake during reactive sputtering growth. In addition, transmission electron microscopy (TEM) and atomic force microscopy (AFM) images for both MBE and sputtered TiN films are shown in Figure S1 (Supporting Information), showing their crystalline properties and surface morphologies.

The dielectric functions (permittivity) of MBE and sputtered TiN films shown in Figure 1c, d are measured by spectroscopic ellipsometry (SE) and fitted by using the Drude–Lorentz model,[43] where the first term (Drude term) represents the contribution from the conduction electrons and the second term (Lorentz term) stands for the interband transitions:

$$\begin{aligned}\varepsilon(\omega) &= \varepsilon_1(\omega) + i\varepsilon_2(\omega)\\ &= \varepsilon_{\mathrm{b}} - \frac{\omega_{\mathrm{p}}^2}{\omega(\omega + i\gamma_{\mathrm{p}})} + \sum_{j=1}^{N} \frac{f_j \tilde{\omega}_j^2}{(\tilde{\omega}_j^2 - \omega^2 - i\omega\Gamma_j)}\end{aligned} \tag{2}$$

where ε_{b} is the polarization response from the core electrons (background permittivity), ω_{p} is the bulk plasmon frequency, γ_{p} is the relaxation rate (electron–electron scattering), f_j and $\tilde{\omega}_j$ are the strengths and resonant frequencies of interband transitions (N is the number of interband transitions used for modeling, N = 3 in this case), and Γ_j is the damping rate of interband transitions.

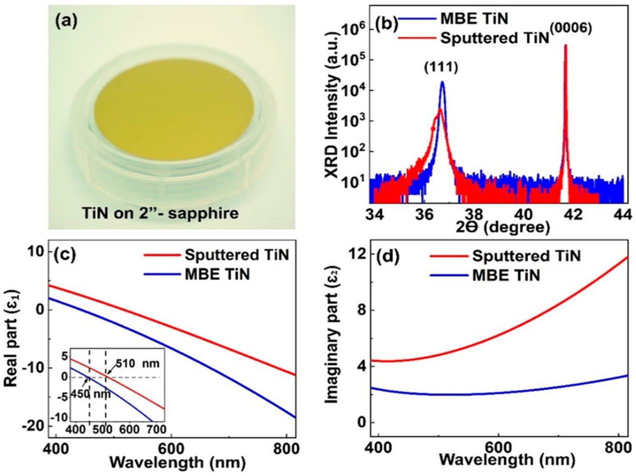

Figure 1. Comparison of optical properties measured for TiN epitaxial films grown by MBE and reactive sputtering on c-plane sapphire substrates. (a) Gold-film-like optical image of TiN epitaxial film grown by MBE with a film thickness of 200 nm. (b) X-ray diffraction patterns (X-ray wavelength: 1.54 Å) show the MBE TiN(111) peak at 36.7° and the sputtered TiN(111) peak at 36.5° with respect to the c-plane sapphire (0006) peak at 41.7°. (c, d) The dielectric functions (ε_1 and ε_2) of TiN films measured by spectroscopic ellipsometry for MBE and sputtered TiN films. According to the SE data, the crossover ($-\varepsilon_1 = 0$) wavelength occurs at λ = 450 nm ($h\nu$ = 2.75 eV) for the MBE TiN film and the λ = 510 nm ($h\nu$ = 2.43 eV) for the sputtered TiN film. The value of the imaginary part (ε_2) measured for the MBE TiN film in the wavelength range of 400–800 nm indicates that it has a lower optical loss.

The real part (ε_1) of the permittivity measured for MBE and sputtered TiN films becomes negative when the wavelength is longer than 450 and 510 nm (crossover wavelength), respectively. Consequently, MBE and sputtered TiN films can be used as a plasmonic metal for wavelengths longer than 450 nm (MBE TiN) or 510 nm (sputtered TiN). The red-shifted crossover wavelength of the sputtered TiN film is in agreement with the formation of titanium oxynitride ($\mathrm{TiO}_x\mathrm{N}_y$), and it can be applied as a tunable plasmonic material with optical properties varied by the oxygen content through reduced conductivity and carrier concentration with increasing oxygen content.[44−46] On the other hand, the imaginary part (ε_2) of the permittivity can be used to measure the degree of optical loss in the film. In this case, the magnitude of ε_2 measured for the sputtered TiN film in the visible range is significantly higher than that of the MBE TiN film, indicating lossy optical properties.

Furthermore, the oxygen-free, stoichiometric nature of the MBE TiN film is confirmed by X-ray photoelectron spectroscopy (XPS) measurements. The surface of as-grown TiN film after exposure to the atmosphere contains a thin titanium oxide surface layer, and the layer thickness is self-limited (i.e., saturated at constant temperature and oxygen partial pressure). This is similar to the case of aluminum film,[47] which can act as a native passivation layer. Figure 2a, b show the Ti 2p XPS spectra at the top film surfaces, which consist of two pairs of Ti $2\mathrm{p}_{3/2}$ and Ti $2\mathrm{p}_{1/2}$ spin–orbit split peaks, where the higher-binding-energy pair can be attributed to the Ti–O bonding and the peak energies correspond closely to the TiO_2 phase with a layer thickness less than the photoelectron escape depth

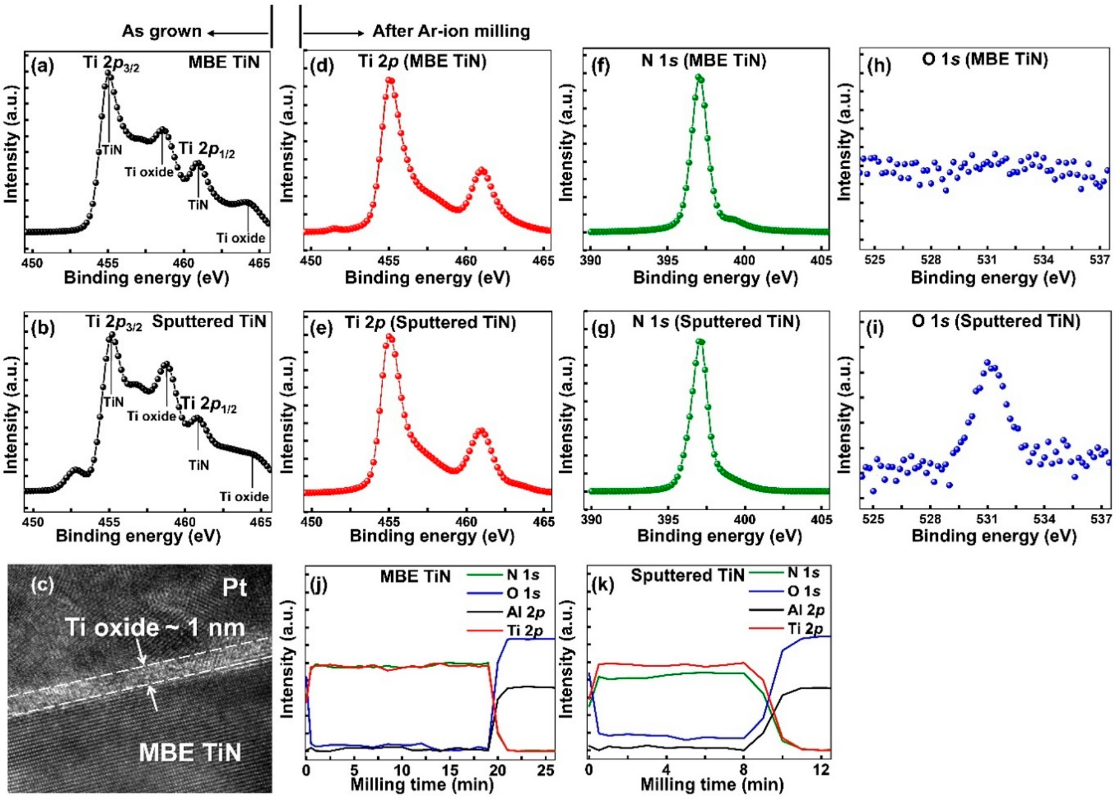

Figure 2. XPS analysis of MBE and sputtered TiN films. (a, b) Ti 2p core-level spectra from the MBE and sputtered TiN films before Ar-ion milling, showing the presence of a TiO_2-like surface layer. (c) High-resolution TEM image reveals the native oxide layer thickness on the MBE TiN film. (d, e) Ti 2p core-level spectra from the MBE and sputtered TiN films after Ar-ion milling show only the TiN-related 2p doublet lines ($2p_{3/2}$, $2p_{1/2}$) with binding energies 455.0 and 461.0 eV. The shakeup peaks at higher binding energies are also visible. (f, g) N 1s core-level spectra show the N 1s binding energies are 397.1 and 397.2 eV for the MBE and sputtered TiN films, respectively. (h, i) N 1s core-level spectra confirm the absence and presence of oxygen after Ar-ion milling inside the MBE and sputtered TiN films. (j, k) Atomic concentration depth profiles with respect to the Ar milling time from top to bottom, The MBE TiN profile shows that the Ti and N concentration is close to 1:1, in contrast to the case of the sputtered TiN film, which has a significant amount of oxygen contamination (i.e., the sputtered film is TiO_xN_{1-x}).

(about a few nanometers). From the XPS peak intensities, it is also evident that the MBE TiN film has a thinner titanium oxide layer thickness. By using the high-resolution TEM image shown in Figure 2c, we confirm that the native titanium oxide layer of the MBE TiN film is about 1−2 nm in thickness.

To reveal the detailed chemical information in the bulk of the TiN films, Ar-ion milling is performed, which also allows for the elemental depth profiles (Ti, O, N) across the film by recording corresponding XPS peak intensities versus the milling time. Figure 2d, e show the Ti 2p XPS spectra in the bulk of MBE and sputtered TiN films, which consist of two pairs of Ti $2p_{3/2}$ and Ti $2p_{1/2}$ spin−orbit split peaks (Ti−N bonding) with electron binding energies of 455.0 and 461.0 eV, respectively. The measured Ti 2p peak energies are in good agreement with that reported for single-crystalline oxygen-free (pristine) TiN measured by XPS.[48] It should be noted that the broad (FWHM ~4 nm) shape-up peaks of Ti−N bonding (shoulder peaks near the Ti $2p_{3/2}$ and Ti $2p_{1/2}$ spin−orbit split peaks at higher binding energies) are spectrally overlapped with the Ti 2p peaks of O−Ti−N bonding. Meanwhile, the nitrogen N 1s XPS peaks have also been investigated by us (shown in Figure 2f, g), and their binding energies are only slightly different: 397.1 (MBE TiN) versus 397.2 eV (sputtered TiN). From the Ti 2p and N 1s XPS results, it is clear that the amount of oxygen in the sputtered TiN film cannot be directly identified by Ti 2p and N 1s XPS measurements. In contrast, the O 1s XPS spectra in the bulk of the TiN films (shown in Figure 2h, i) can precisely determine the absence (MBE TiN) and presence (sputtered TiN) of the oxygen content. During Ar-ion milling of MBE and sputtered TiN films, we have also recorded the concentration depth profiles of Ti, O, N, and Al from the top of the film to the sapphire substrate, which are shown in Figure 2j, k. It can be clearly seen that the atomic concentrations of Ti and N in MBE TiN are close to 1:1, while the element composition of the sputtered TiN film is close to TiO_xN_{1-x} ($x \approx 0.1$−0.2).

Herein, we also demonstrate the TiN metasurface broadband absorber for high-temperature applications. In Figure 3a, the single-TiN-layer metasurface structure is schematically shown. The nanohole array structure is chosen because of its simplicity and good performance. Moreover, the single-TiN-layer metasurface requires a less complicated fabrication process, as compared to the common metal insulator metal (MIM)-based perfect absorber. On such an array, nanoholes are periodically distributed in both x and y directions with specifically designed hole pitch, diameter, and depth for optimized broadband absorption over the full visible spectral region. Figure 3b shows the SEM image of the actual TiN metasurface fabricated by electron beam lithography (see Methods and Figure S2 in the Supporting Information for experimental details). This TiN metasurface absorber is

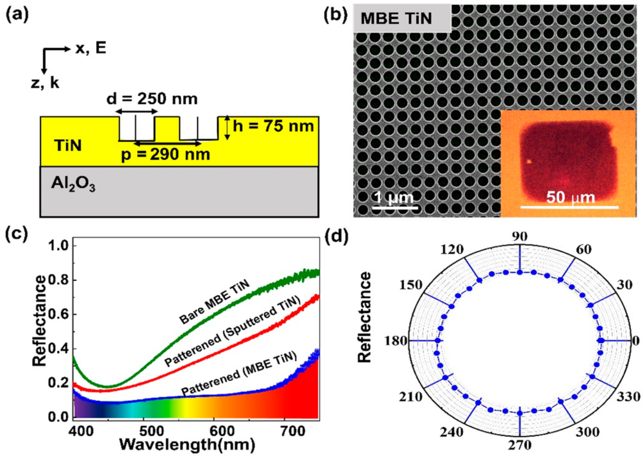

Figure 3. TiN metasurface solar absorber. (a) Schematic representation of the absorber consisting of a TiN nanohole array with optimized structural parameters: pitch (p) = 290, diameter (d) = 250 nm, and height (h) = 75 nm. The MBE-grown TiN epitaxial film was grown on a sapphire wafer with a film thickness of 200 nm. (b) SEM image of the TiN nanohole array; inset shows an optical microscope image of the nanohole array, demonstrating a strong absorption in the full visible range. (c) Comparison spectra of optical absorbance measured for the MBE TiN metasurface (blue), the sputtered TiN metasurface (red) using the same nanoholes array structure, and a bare MBE TiN film (green). (d) Polarized reflectance plot measured for the MBE TiN metasurface confirms that the broadband optical absorption is insensitive to the incident light polarization.

polarization independent at normal incidence of incident light. The perfect ("dark") absorber nature of the TiN metasurface is shown in the inset of Figure 3b, which is an optical microscope image using an unpolarized white light.

In comparison, we measure reflectance spectra (Figure 3c) of as-fabricated metasurfaces made from MBE and sputtered TiN films, as well as a bare MBE TiN film. The absorbance (A) of the metasurface can be derived from $1 - R$, where R is the reflectance since transmittance is zero due to the absorbing nature of the metallic film with a sufficient thickness. Note that this assumption is not valid at wavelengths shorter than the crossover wavelength (~450 nm for the MBE TiN film) as the film is no longer metallic, as shown in Figure 3c for the case of bare MBE TiN film (green curve). In Figure 3c, the blue curve represents experimental reflectance spectra of the MBE TiN metasurface, and the absorption is found to be ~90% over the visible range. By contrast, the sputtered TiN metasurface shows a lower absorption (red curve) due to the oxidized nature of sputtered TiN confirmed by XPS analysis. Furthermore, Figure 3d shows a polarized reflectance plot measured for the MBE TiN metasurface, confirming that optical absorption is insensitive to the incident light polarization.

To explain the optical multiresonance behavior (broadband response) of a TiN metasurface absorber, we have analyzed the electric field distributions of a MBE TiN metasurface broadband absorber by using the FDTD method. Figure 4 shows the electric field intensity profiles of the electric field (z component) on the x−y plane and on the x−z plane for a single nanohole at different wavelengths (linearly polarized incident light at 500, 600, and 700 nm). It is clear that multiresonance occurs at a broad range of wavelengths. Moreover, the phase switching behavior that occurs from 600 to 700 nm indicates that multiresonance can be related to cross-coupling among nanoholes. Therefore, we believe that the multiresonant behavior is the origin of broadband absorption from 500 to 750 nm.

For STPV applications, demanding high-temperature oxidation-resistant operation is compulsory in order to conclude their suitability, which requires highly concentrated sunlight. The concentrated sunlight can be converted into heat, and the local heating effects cause material damage before the average temperature reaches close to the melting point of the TiN metasurface. To evaluate the stable performance of the TiN metasurface absorber, we use a solar simulator at different irradiation intensities of 70 suns (7 W/cm^2), 90 suns (9 W/cm^2), and 130 suns (13 W/cm^2) in a wavelength range of 400−1200 nm. The MBE and sputtered TiN metasurface

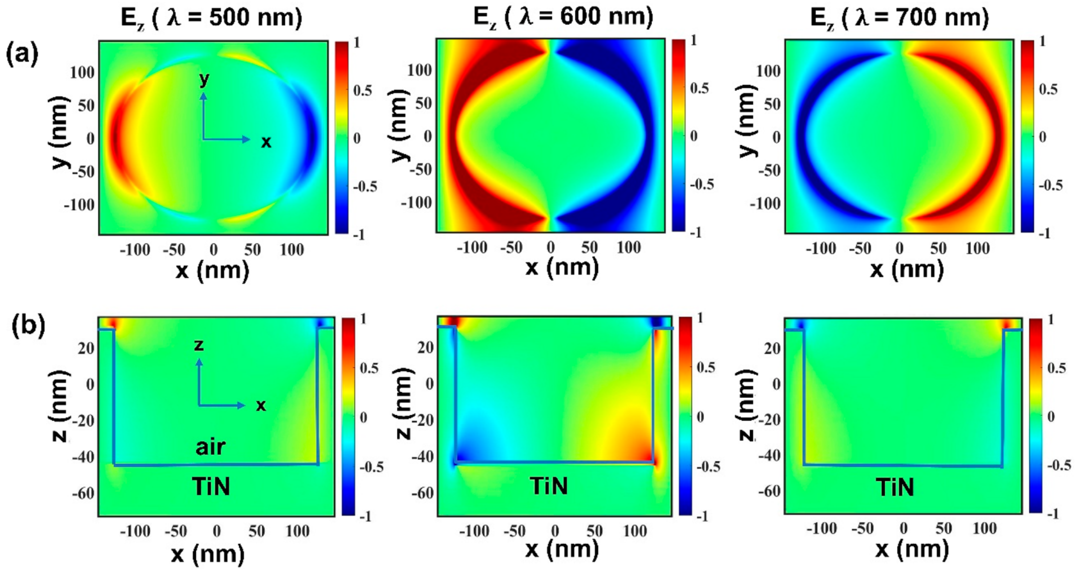

Figure 4. FDTD simulations. (a) and (b) Electric field distribution of the TiN metasurface broadband absorber along the z axis component plotted on the x−y and x−z plane at different incident light wavelengths (500, 600, and 700 nm).

absorbers are exposed to the solar simulator in the ambient environment at these irradiation intensities for 6 h. Notably, the stoichiometric MBE TiN metasurface absorber can progressively tolerate the sun irradiation up to 13 W/cm^2 (130 suns) for 6 h, as shown in the Figure 5a. In contrast, Figure S3a (Supporting Information) reveals that the sputtered TiN absorber starts to be damaged when the irradiation reaches an intensity of 130 suns.

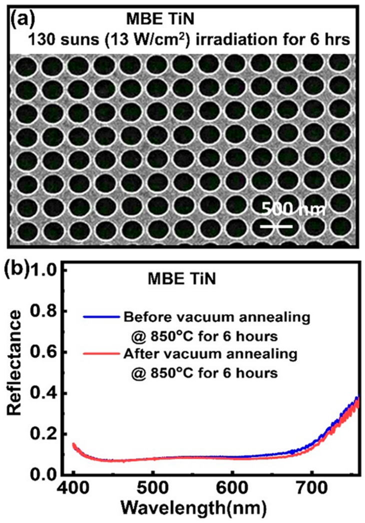

Figure 5. Thermal stability of the MBE TiN broadband absorber. (a) SEM image of the MBE TiN absorber under sun irradiation at an intensity of 130 suns (13 W/cm^2) for 6 h. (b) Measured absorption spectra of the MBE TiN absorber before and after vacuum annealing at 850 °C for 6 h.

In addition, we have also compared the thermal stability of two different TiN absorbers. For this purpose, we heat the MBE and sputtered TiN metasurface absorbers in an ultrahigh vacuum chamber at three temperatures (600, 700, and 850 °C) for 6 h. In this experiment, the MBE and sputtered TiN absorbers retain their morphology and optical performance after annealing at 600 and 700 °C. However, after both metasurfaces are heated at 850 °C for 6 h, major differences start to appear. While there is no change for the case of the MBE TiN metasurface absorber, as demonstrated in Figure 5b, the sputtered TiN metasurface absorber has a drastic morphology change, and the optical properties have also been affected (Figure S3b, c in the Supporting Information). This is likely due to the significant oxygen content in the sputtered TiN film, which can seriously degrade the thermal stability.

■ CONCLUSIONS

In this work, we demonstrate a refractory, single-layer, and polarization-independent metasurface broadband absorber over the visible spectrum using the single-crystalline oxygen-free TiN film grown by nitrogen-plasma-assisted MBE. This metasurface absorber is easy to fabricate and possesses some important advantages as compared to the traditional MIM absorber structure, which is more complicated to fabricate, and the inclusion of the insulating oxide layer might not support high-temperature operation. In comparison with the TiN epitaxial film prepared by the reactive sputtering method, the XRD, TEM, SE, and XPS measurement results confirm that the MBE TiN epitaxial film has better crystalline and optical properties, as well as an oxygen-free stoichiometric composition. As an important consequence, the MBE TiN epitaxial film exhibits excellent thermal and chemical stabilities under high-temperature annealing in vacuum and high solar irradiance, which make it a promising material for demanding high-temperature applications such as solar thermophovoltics.

■ ASSOCIATED CONTENT

Supporting Information

The Supporting Information is available free of charge at https://pubs.acs.org/doi/10.1021/acs.jpcc.1c03053.

> TEM and AFM images for both MBE and sputtered TiN films (Figure S1), flowchart of the TiN metasurface fabrication process (Figure S2), and thermal instability of the sputtered TiN solar absorber under sun irradiation in the ambient environment, confirmed by SEM images and optical measurements (Figure S3) (PDF)

■ AUTHOR INFORMATION

Corresponding Author

Shangjr Gwo − *Institute of NanoEngineering and MicroSystems and Department of Physics, National Tsing-Hua University, Hsinchu 30013, Taiwan; Research Center for Applied Sciences, Academia Sinica, Nankang, Taipei 11529, Taiwan;* orcid.org/0000-0002-3013-0477; Email: gwo@phys.nthu.edu.tw

Authors

Ragini Mishra − *Institute of NanoEngineering and MicroSystems, National Tsing-Hua University, Hsinchu 30013, Taiwan*

Ching-Wen Chang − *Research Center for Applied Sciences, Academia Sinica, Nankang, Taipei 11529, Taiwan;* orcid.org/0000-0002-1748-4983

Abhishek Dubey − *Department of Materials Science and Engineering, National Tsing-Hua University, Hsinchu 30013, Taiwan*

Zong-Yi Chiao − *Department of Physics, National Taiwan University, Taipei 10617, Taiwan*

Ta-Jen Yen − *Department of Materials Science and Engineering, National Tsing-Hua University, Hsinchu 30013, Taiwan;* orcid.org/0000-0003-3613-699X

Ho Wai Howard Lee − *Department of Physics and Astronomy, University of California, Irvine, California 92697-4575, United States;* orcid.org/0000-0003-3962-3726

Yu-Jung Lu − *Research Center for Applied Sciences, Academia Sinica, Nankang, Taipei 11529, Taiwan; Department of Physics, National Taiwan University, Taipei 10617, Taiwan;* orcid.org/0000-0002-3932-653X

Complete contact information is available at: https://pubs.acs.org/10.1021/acs.jpcc.1c03053

Notes

The authors declare no competing financial interest.

■ ACKNOWLEDGMENTS

SE measurements, electron beam lithography, and TCP-RIE etching were performed in the Taiwan Semiconductor Research Institute (TSRI), Hsinchu. S.G. and Y.J.L. acknowledge the Ministry of Science and Technology in Taiwan for funding support (MOST-109-2123-M-007-001 (S.G.), MOST-107-2923-M-007-004-MY3 (S.G.), and MOST-109-2112-M-001-043-MY3 (Y.J.L.)). H.W.H.L. acknowledge funding support from AFOSR-AOARD (award no. FA2386-18-1-4099) and National Science Foundation (grant no. 1752295).

■ REFERENCES

(1) Shockley, W.; Queisser, H. J. Detailed balance limit of efficiency of p−n junction solar cells. *J. Appl. Phys.* **1961**, *32*, 510−519.

(2) Swanson, R. M. A proposed thermophotovoltaic solar energy conversion system. *Proc. IEEE* **1979**, *67*, 446−447.

(3) Spirkl, W.; Ries, H. Solar thermophotovoltaics: an assessment. *J. Appl. Phys.* **1985**, *57*, 4409−4414.

(4) Davies, P. A.; Luque, A. Solar thermophotovoltaics: brief review and a new look. *Sol. Energy Mater. Sol. Cells* **1994**, *33*, 11−22.

(5) Rephaeli, E.; Fan, S. Absorber and emitter for solar thermophotovoltaic systems to achieve efficiency exceeding the Shockley-Queisser limit. *Opt. Express* **2009**, *17*, 15145−15159.

(6) Kraemer, D.; Poudel, B.; Feng, H.-P.; Caylor, J. C.; Yu, B.; Yan, X.; Ma, Y.; Wang, X.; Wang, D.; Muto, A.; et al. High-performance flat-panel solar thermoelectric generators with high thermal concentration. *Nat. Mater.* **2011**, *10*, 532−538.

(7) Lenert, A.; Bierman, D. M.; Nam, Y.; Chan, W. R.; Celanović, I.; Soljačić, M.; Wang, E. N. A nanophotonic solar thermophotovoltaic device. *Nat. Nanotechnol.* **2014**, *9*, 126−130.

(8) Fan, S. An alternative "sun" for solar cells. *Nat. Nanotechnol.* **2014**, *9*, 92−93.

(9) Ungaro, C.; Gray, S. K.; Gupta, M. C. Solar thermophotovoltaic system using nanostructures. *Opt. Express* **2015**, *23*, A1149−A1156.

(10) Omair, Z.; Scranton, G.; Pazos-Outón, L. M.; Xiao, T. P.; Steiner, M. A.; Ganapati, V.; Peterson, P. F.; Holzrichter, J.; Atwater, H.; Yablonovitch, E. Ultraefficient thermophotovoltaic power conversion by band-edge spectral filtering. *Proc. Natl. Acad. Sci. U. S. A.* **2019**, *116*, 15356−15361.

(11) Wang, Y.; Liu, H.; Zhu, J. Solar thermophotovoltaics: Progress, challenges, and opportunities. *APL Mater.* **2019**, *7*, 080906.

(12) Harder, N.-P.; Würfel, P. Theoretical limits of thermophotovoltaic solar energy conversion. *Semicond. Sci. Technol.* **2003**, *18*, S151−S157.

(13) Buddhiraju, S.; Santhanam, P.; Fan, S. Thermodynamic limits of energy harvesting from outgoing thermal radiation. *Proc. Natl. Acad. Sci. U. S. A.* **2018**, *115*, E3609−E3615.

(14) Atwater, H. A.; Polman, A. Plasmonics for improved photovoltaic devices. *Nat. Mater.* **2010**, *9*, 205−213.

(15) Boltasseva, A.; Atwater, H. A. Low-loss plasmonic metamaterials. *Science* **2011**, *331*, 290−291.

(16) Guler, U.; Boltasseva, A.; Shalaev, V. M. Refractory plasmonics. *Science* **2014**, *344*, 263−264.

(17) Li, W.; Guler, U.; Kinsey, N.; Naik, G. V.; Boltasseva, A.; Guan, J.; Shalaev, V. M.; Kildishev, A. V. Refractory plasmonics with titanium nitride: broadband metamaterial absorber. *Adv. Mater.* **2014**, *26*, 7959−7965.

(18) Wang, H.; Chen, Q.; Wen, L.; Song, S.; Hu, X.; Xu, G. Titanium-nitride-based integrated plasmonic absorber/emitter for solar thermophotovoltaic application. *Photonics Res.* **2015**, *3*, 329−334.

(19) Chirumamilla, M.; Chirumamilla, A.; Yang, Y.; Roberts, A. S.; Kristensen, P. K.; Chaudhuri, K.; Boltasseva, A.; Sutherland, D. S.; Bozhevolnyi, S. I.; Pedersen, K. Large-area ultrabroadband absorber for solar thermophotovoltaics based on 3D titanium nitride nanopillars. *Adv. Opt. Mater.* **2017**, *5*, 1700552.

(20) Huo, D.; Zhang, J.; Wang, H.; Ren, X.; Wang, C.; Su, H.; Zhao, H. Broadband perfect absorber with monolayer MoS_2 and hexagonal titanium nitride nano-disk array. *Nanoscale Res. Lett.* **2017**, *12*, 465.

(21) Yang, Z.-Y.; Ishii, S.; Doan, A. T.; Shinde, S. L.; Dao, T. D.; Lo, Y.-P.; Chen, K.-P.; Nagao, T. Narrow-band thermal emitter with titanium nitride thin film demonstrating high temperature stability. *Adv. Opt. Mater.* **2020**, *8*, 1900982.

(22) Patsalas, P.; Logothetidis, S. Optical, electronic, and transport properties of nanocrystalline titanium nitride thin films. *J. Appl. Phys.* **2001**, *90*, 4725−4734.

(23) Cortie, M. B.; Giddings, J.; Dowd, A. Optical properties and plasmon resonances of titanium nitride nanostructures. *Nanotechnology* **2010**, *21*, 115201.

(24) Naik, G. V.; Schroeder, J. L.; Ni, X.; Kildishev, A. V.; Sands, T. D.; Boltasseva, A. Titanium nitride as a plasmonic material for visible and near-infrared wavelengths. *Opt. Mater. Express* **2012**, *2*, 478−489.

(25) Patsalas, P.; Kalfagiannis, N.; Kassavetis, S. Optical properties and plasmonic performance of titanium nitride. *Materials* **2015**, *8*, 3128−3154.

(26) Kumar, M.; Umezawa, N.; Ishii, S.; Nagao, T. Examining the performance of refractory conductive ceramics as plasmonic materials: A theoretical approach. *ACS Photonics* **2016**, *3*, 43−50.

(27) Murai, S.; Fujita, K.; Daido, Y.; Yasuhara, R.; Kamakura, R.; Tanaka, K. Plasmonic arrays of titanium nitride nanoparticles fabricated from epitaxial thin films. *Opt. Express* **2016**, *24*, 1143−1153.

(28) Catellani, A.; Calzolari, A. Plasmonic properties of refractory titanium nitride. *Phys. Rev. B: Condens. Matter Mater. Phys.* **2017**, *95*, 115145.

(29) Zgrabik, C. M.; Hu, E. L. Optimization of sputtered titanium nitride as a tunable material for plasmonic applications. *Opt. Mater. Express* **2015**, *5*, 2786−2797.

(30) Guo, W.-P.; Mishra, R.; Cheng, C.-W.; Wu, B.-H.; Chen, L.-J.; Lin, M.-T.; Gwo, S. Titanium nitride epitaxial films as a plasmonic material platform: Alternative to gold. *ACS Photonics* **2019**, *6*, 1848−1854.

(31) Diroll, B. T.; Saha, S.; Shalaev, V. M.; Boltasseva, A.; Schaller, R. D. Broadband ultrafast dynamics of refractory metals: TiN and ZrN. *Adv. Opt. Mater.* **2020**, *8*, 2000652.

(32) Guler, U.; Ndukaife, J. C.; Naik, G. V.; Nnanna, A. G. A.; Kildishev, A. V.; Shalaev, V. M.; Boltasseva, A. Local heating with lithographically fabricated plasmonic titanium nitride nanoparticles. *Nano Lett.* **2013**, *13*, 6078−6083.

(33) Reddy, H.; Guler, U.; Kudyshev, Z.; Shalaev, V. M.; Boltasseva, A.; Kildishev, A. V. Temperature-dependent optical properties of plasmonic titanium nitride thin films. *ACS Photonics* **2017**, *4*, 1413−1420.

(34) Briggs, J. A.; Naik, G. V.; Zhao, Y.; Petach, T. A.; Sahasrabuddhe, K.; Goldhaber-Gordon, D.; Melosh, N. A.; Dionne, J. A. Temperature-dependent optical properties of titanium nitride. *Appl. Phys. Lett.* **2017**, *110*, 101901.

(35) Wells, M. P.; Bower, R.; Kilmurray, R.; Zou, B.; Mihai, A. P.; Gobalakrichenane, G.; Alford, A. M.; Oulton, R. F. M.; Cohen, L. F.; Maier, S. A.; et al. Temperature stability of thin film refractory plasmonic materials. *Opt. Express* **2018**, *26*, 15726−15744.

(36) Gadalla, M. N.; Greenspon, A. S.; Tamagnone, M.; Capasso, F.; Hu, E. L. Excitation of strong localized surface plasmon resonances in highly metallic titanium nitride nano-antennas for stable performance at elevated temperatures. *ACS Appl. Nano Mater.* **2019**, *2*, 3444−3452.

(37) Mascaretti, L.; Dutta, A.; Kment, Š.; Shalaev, V. M.; Boltasseva, A.; Zbořil, R.; Naldoni, A. Plasmon-enhanced photoelectrochemical water splitting for efficient renewable energy storage. *Adv. Mater.* **2019**, *31*, 1805513.

(38) Naldoni, A.; Kudyshev, Z. A.; Mascaretti, L.; Sarmah, S. P.; Rej, S.; Froning, J. P.; Tomanec, O.; Yoo, J. E.; Wang, D.; Kment, Š.; et al. Solar thermoplasmonic nanofurnace for high-temperature heterogeneous catalysis. *Nano Lett.* **2020**, *20*, 3663−3672.

(39) Vasile, M. J.; Emerson, A. B.; Baiocchi, F. A. The characterization of titanium nitride by x-ray photoelectron spectroscopy and Rutherford backscattering. *J. Vac. Sci. Technol., A* **1990**, *8*, 99−105.

(40) Saha, N. C.; Tompkins, H. G. Titanium nitride oxidation chemistry: An x-ray photoelectron spectroscopy study. *J. Appl. Phys.* **1992**, *72*, 3072−3079.

(41) Gwo, S.; Yeh, C.-L.; Chen, P.-F.; Chou, Y.-C.; Chen, T. T.; Chao, T.-S.; Hu, S.-F.; Huang, T.-Y. Local electric-field-induced oxidation of titanium nitride films. *Appl. Phys. Lett.* **1999**, *74*, 1090−1092.

(42) Zhang, R.; Ma, Q.-Y.; Liu, H.; Sun, T.-Y.; Bi, J.; Song, Y.; Peng, S.; Liang, L.; Gao, J.; Cao, H.; et al. Crystal orientation-dependent oxidation of epitaxial TiN films with tunable plasmonics. *ACS Photonics* **2021**, *8*, 847−856.

(43) Langereis, E.; Heil, S. B. S.; van de Sanden, M. C. M.; Kessels, W. M. M. *In situ* spectroscopic ellipsometry study on the growth of ultrathin TiN films by plasma-assisted atomic layer deposition. *J. Appl. Phys.* **2006**, *100*, 023534.

(44) Graciani, J.; Hamad, S.; Sanz, J. F. Changing the physical and chemical properties of titanium oxynitrides $TiN_{1-x}O_x$ by changing the composition. *Phys. Rev. B: Condens. Matter Mater. Phys.* **2009**, *80*, 184112.

(45) Lu, Y.-J.; Sokhoyan, R.; Cheng, W.-H.; Shirmanesh, G. K.; Davoyan, A. R.; Pala, R. A.; Thyagarajan, K.; Atwater, H. A. Dynamically controlled Purcell enhancement of visible spontaneous emission in a gated plasmonic heterostructure. *Nat. Commun.* **2017**, *8*, 1631.

(46) Braic, L.; Vasilantonakis, N.; Mihai, A.; Villar Garcia, I. J.; Fearn, S.; Zou, B.; Alford, N. M.; Doiron, B.; Oulton, R. F.; Maier, S. A.; et al. Titanium oxynitride thin films with tunable double epsilon-near-zero behavior for nanophotonic applications. *ACS Appl. Mater. Interfaces* **2017**, *9*, 29857−29862.

(47) Nguyen, L.; Hashimoto, T.; Zakharov, D. N.; Stach, E. A.; Rooney, A. P.; Berkels, B.; Thompson, G. E.; Haigh, S. J.; Burnett, T. L. Atomic-scale insights into the oxidation of aluminium. *ACS Appl. Mater. Interfaces* **2018**, *10*, 2230−2235.

(48) Jaeger, D.; Patscheider, J. Single crystalline oxygen-free titanium nitride by XPS. *Surf. Sci. Spectra* **2013**, *20*, 1−8.